

PCCP

Accepted Manuscript



This is an *Accepted Manuscript*, which has been through the Royal Society of Chemistry peer review process and has been accepted for publication.

Accepted Manuscripts are published online shortly after acceptance, before technical editing, formatting and proof reading. Using this free service, authors can make their results available to the community, in citable form, before we publish the edited article. We will replace this *Accepted Manuscript* with the edited and formatted *Advance Article* as soon as it is available.

You can find more information about *Accepted Manuscripts* in the [Information for Authors](#).

Please note that technical editing may introduce minor changes to the text and/or graphics, which may alter content. The journal's standard [Terms & Conditions](#) and the [Ethical guidelines](#) still apply. In no event shall the Royal Society of Chemistry be held responsible for any errors or omissions in this *Accepted Manuscript* or any consequences arising from the use of any information it contains.

Effect of Lipid Head Group Interactions in Membrane Properties and Membrane-Induced Cationic β -Hairpin Folding[†]

Sai J Ganesan,^{a,c} Hongcheng Xu,^{b,c} and Silvina Matysiak^{*d}

Membrane interfaces (mIFs) are ubiquitous components of living cells and are host to many essential biological processes. One key characteristic of mIFs is the dielectric gradient and subsequently, electrostatic potential that arises from dipolar interactions in the head group region. In this work, we present a coarse-grained (CG) model for anionic and zwitterionic lipids that accounts for dipolar intricacies in the head group region. Prior work on adding dipolar interactions in a coarse grained (CG) model for peptides enabled us to achieve α/β secondary structure content *de novo*, without any added bias. We have now extended this idea to lipids. To mimic dipolar interactions, two dummy particles with opposite charges are added to CG polar beads. These two dummy charges represent a fluctuating dipole that introduces structural polarization into the head group region. We have used POPC (1-palmitoyl-2-oleoyl-*sn*-glycero-3-phosphocholine) and POPS (1-palmitoyl-2-oleoyl-*sn*-glycero-3-phospho-L-serine) as our model lipids. We characterize structural, dynamic, and dielectric properties of our CG bilayer, along with the effect of monovalent ions. We observe head group dipoles to play a significant role in membrane dielectric gradient and lipid clustering induced by dipole-dipole interactions in POPS lipids. In addition, we have studied membrane-induced peptide folding of a cationic antimicrobial peptide with anticancer activity, SVS-1. We find that membrane-induced peptide folding is driven by both (a) cooperativity in peptide self interaction and (b) cooperativity in membrane-peptide interaction. In particular, dipolar interactions between peptide backbone and lipid head groups contribute to stabilizing folded conformations.

1 INTRODUCTION

Zwitterionic phospholipid phosphatidylcholine (PC), and anionic phospholipid phosphatidylserine (PS) comprise 40-55% and 3-10% respectively, of total mammalian cell membrane phospholipids¹. Their structural and dynamical properties have been found to play important roles in a number of biological processes. Electrostatic interactions between lipid head groups have an effect on a membrane's internal electrical dipole potential, which varies from 100 mV to 400 mV, depending on the composition of lipids². This dipole potential has also been shown to dramatically impact ion channel permeability in biological membranes³.

Biological membrane interfaces (mIF) provide a unique dielectric environment in which proteins undergo conformational transitions from a water-soluble to a membrane associated state^{4,5}. Short model peptides, especially antimicrobial peptides (AMPs), have been extremely useful in characterizing energetics of interfacial folding^{6,7}. AMPs are cationic peptides with a significant level of hydrophobicity. Anticancer peptides (ACP) are AMPs designed to target tumor cells, one such *de novo* designed ACP is SVS-1 (KVKVKVKV^DP^LPTKVKVKVK – NH₂)⁸. SVS-1, like

AMPs, are disordered in the aqueous phase (bioinactive), but is fully structured upon partitioning onto an interface (bioactive)⁸. This ACP is known to fold into a β -sheet on interaction with negatively charged vesicles⁸. The literature on experimental and computational characterization of biophysical properties of AMPs is vast⁹⁻¹². It has been proposed that the energetic cost of partitioning unfolded peptides into mIFs is reduced by secondary structure formation or intermolecular hydrogen bonds¹³. Membrane lipid composition is known to play a crucial role as well; for example, differences in the amount of acidic membrane phospholipids and cholesterol are known to play a critical role in specificity of magainins^{14,15}. However, the balance of driving forces between the two states (water soluble and membrane bound) remains to be understood. Coarse-grained membrane models that capture the right dielectric gradient, and peptide models that can capture protein secondary structures should have essential ingredients to decode such a process.

Molecular simulations are being increasingly used to improve our knowledge of microscopic phenomena^{16,17}. Atomistic simulations have contributed to the understanding of many membrane processes¹⁸⁻²², including the existence of anionic lipid clusters, mediated by ion-dipole or hydrogen bond (a type of dipole-dipole interaction) networks in both mono-component and mixed bilayers²³⁻²⁵. It has been hypothesized that these clusters could be intermediate structures on pathway to experimentally observed lipid phase separation in mixed PC/PS bilayers on longer time scales.²⁶

Unlike atomistic simulations, coarse-grained (CG) models aid in both exploring larger length and time scale molecular phenomena, and in narrowing down the key interactions re-

[†] Electronic Supplementary Information (ESI) available:

^a Department of Bioengineering, University of Maryland, College Park, Maryland, USA.

^b Biophysics Program, University of Maryland, College Park, Maryland, USA.

^d Department of Bioengineering and Biophysics Program, University of Maryland, College Park, Maryland, USA. Tel: 301 405 0313; E-mail: matysiak@umd.edu

^c S. J. Ganesan and H. C. Xu contributed equally to this work.

sponsible for significant system characteristics. CG simulations of lipid systems have largely proven to be efficient in giving us a thorough and coherent picture of membrane structure and have been used in the past to explore lipid domain formation in mixed bilayers for systems that do not have anionic lipids^{27–29}. There exist a large number of CG models that have yielded significant results and extended our understanding of membrane molecular processes^{30–35}. Among them, a transferable model called MARTINI force field^{34,35}, built on thermodynamic data of oil/water partitioning coefficient, achieves a broader range of applications without the need for re-parametrization.

In this work, we present a CG lipid model that can be used to explore the role of head group dipoles in membrane structure and interfacial peptide folding. This model has roots in the MARTINI force field, and is combined with a new Water-Explicit Polarizable PROtein Model (WEPPROM) developed by some of us³⁶ and Yesylevskyy's polarizable water model³⁷. By modeling a protein backbone bead as a flexible dipole, we were able to achieve *de novo* helix and sheet content without any biases. In WEPPROM, the dipolar interactions can be considered as pseudo hydrogen bonds, which contribute to cooperativity in folding secondary and supersecondary structures. An analog to our model is the multipole CG model developed by Ren et al.

In this work, we have added structural polarization to polar groups of a lipid model, to capture the dipole interactions that can exist in the head group region of anionic bilayers. The change in orientation of atoms underlying polar CG units of the lipids are captured by a flexible dipole inside each polar CG unit. This flexible dipole is created by angular changes in oppositely charged dummy or dipolar particles, which are constrained to the center of mass site. Dipolar particles interact with each other and with charged beads through Coulombic potentials, introducing structural polarization into the model.

We have chosen a zwitterionic lipid, 1-palmitoyl-2-oleoyl-*sn*-glycerol-3-phosphatidylcholine (POPC), and an anionic lipid, 1-palmitoyl-2-oleoyl-*sn*-glycerol-3-phosphatidylserine (POPS), as model lipids. The choice of the above two lipids is governed by the use of POPC/POPS mixed systems as common models in the study of plasma membranes^{38,39}. In this paper, we explore (a) the role of head group dipole interactions in membrane structure and dynamics, (b) the effect of monovalent ions on lipid dipole interactions and bilayer properties, and (c) membrane-induced folding of SVS-1.

2 METHODS

2.1 Lipid Model

A mapping scheme consistent with the MARTINI model for POPC and POPS lipids is used, and is shown in Figure 1a. A

phospholipid molecule is mapped onto a structure consisting of 13 CG sites made of 3 different bead types. The bead types used are: charged (*C*), polarizable (*Pol*), and hydrophobic (*H*). We also use a set of bead subtypes similar to the MARTINI force field, with distinct modifications in the Lennard-Jones (LJ) parameters, to account for all the CG sites. *C0*, *C+* and *C-* are charged bead subtypes, where *C+* is a representative hydrogen bond donor, *C-* acceptor, and *C0* is neither. *Pol1* and *Pol2* are subtypes of the polarizable bead, sorted in order of decreasing polarity. *H1* and *H2* are subtypes of the hydrophobic bead, in decreasing order of hydrophobicity. As depicted in Figure 1a, the PC head group region consists of two hydrophilic groups: choline (NC3) and phosphate (PO4) with *C0* and *C-* bead types respectively. The PS head group region also consists of two hydrophilic groups: serine (CNO) with oppositely charged dummy particles (CNM and CNP), as shown in Figure 1b, and phosphate (PO4), with *Pol1* and *C-* bead subtypes respectively. For both lipids, two sites of intermediate hydrophilicity (bead subtype *Pol2*) are used to represent the glycerol ester groups (GL1 and GL2), each with oppositely charged dummy particles (G1M, G1P and G2M, G2P), as shown in Figure 1b. The oleoyl tail is modeled with 5 beads, 4 of *H1* subtype and a central bead of *H2* subtype (a less hydrophobic bead to model the double bond). The palmitoyl tail is modeled with 4 beads of subtype *H1*. All ions used are modeled as hydrated ions with a point charge, using charged bead subtypes *C+* or *C-*

The CG phospholipid model is combined with the polarizable coarse-grained (pCG) water model developed by Yesylevskyy et al.³⁷. The pCG bead of our lipid model consists of three interaction sites, of which one is the center of mass site and the other two are dummy particles with opposite charges, as depicted in Figure 1b. The dummies are added into the polarizable bead only to create a flexible dipole which interacts with other particles via electrostatic interactions. The Lennard-Jones pairwise interactions are defined between the main CG sites. A constraint with a distance (*l*) is defined between dummies and the main site, and all the three interaction sites are bound by a cosine squared angle potential (equilibrium angle θ and angular force constant k_θ) to control the rotation of dummy particles. To avoid overpolarization, a small repulsive core is added to dummy particles, as commonly done in polarizable all-atom force fields⁴⁰. All 1-2 non-bonded interactions are excluded between the main CG sites and their corresponding embedded dipole particles. In addition, the non-bonded interactions between dummy particles inside a polarizable bead are excluded as well. The mass of a CG bead (72 a.m.u) is distributed equally among the three particles (24 a.m.u. each) in polarizable beads.

Table 1 Table of vaporization, hydration and partition free energy in kcal/mol. The partition free energy is evaluated for water/hexadecane interface. ΔG^M is the free energy calculated using the MARTINI model³⁴, ΔG^P , with our water-explicit polarizable coarse-grained model, and ΔG^E is the free energy from experiment³⁴.

Bead	Chemistry	Examples	ΔG_{vap}^M	ΔG_{vap}^P	ΔG_{vap}^E	ΔG_{hyd}^M	ΔG_{hyd}^P	ΔG_{hyd}^E	ΔG_{part}^M	ΔG_{part}^P	ΔG_{part}^E
C0	C ₃ N ⁺	choline	-	-	-	-6.0	-6.0	-	<-7.2	<-7.2	-
C+	H ₃ N ⁺ -C ₃	1-propylamine	-	-	-	-6.0	-6.0	-	<-7.2	<-7.2	-
C-	PO ₄ ⁻	phosphate	-	-	-	-6.0	-6.0	-	<-7.2	<-7.2	-
Pol1	H ₂ N-C ₂ =O	acetamide	sol	sol	sol	-6.7	-6.9	-9.6	-6.7	-6.9	-6.5
Pol2	C-O-C=O	methylformate	-3.1	-2.2	-3.8~5.5	-2.2	-2.4	-2.9~-3.8	-1.7	-1.9	-1.0~-1.4
H1	C ₄	butane	-2.4	-2.4	-2.6	3.3	4.5	2.2~2.4	4.3	5.0	4.3
H2	C ₂ =C ₂	2-butene	-2.4	-2.4	-3.8	1.2	3.8	-0.2~-0.5	3.1	4.1	2.9

2.2 Lipid Force Field Parameters

Our force field consists of bonded (harmonic bond and angular potential for lipid and peptide) and non-bonded terms (Lennard-Jones and Coulombic potentials). All non-dipolar bonded interactions are based on the MARTINI force field^{34,35}, and are fine-tuned using MARTINI's LJ parameter scale as a baseline. The bonded distance between two adjacent head group beads is 0.37 nm and between adjacent tail beads is 0.47 nm, both with a bond strength of 298.8 kcal/mol. The only angle defined among head groups are between the phosphate and ester beads (PO4-GL1-GL2), which is set to 120°. Angles involving tail groups are set to 180°. The interaction strength of both the angles are set to 6.0 kcal/mol. There is an exception for the double bond in the carbon tail, which is set to 120° with an interaction strength of 10.8 kcal/mol.

The parametrization of non-bonded terms is done in two stages to account for (a) thermodynamic parameters or free energy values of partitioning, hydration, and vaporization of each bead type, and (b) dipole moments of polarizable beads. The dipole moment of polarizable beads is initially parameterized to match that of the corresponding chemical group in atomistic detail from all-atom simulations. There are four parameters for the polarizable CG bead that can be tuned to obtain the desired average dipole moment (l, q, θ, k_θ). Since the polarization of the bead inevitably adds extra electrostatic interactions to the system, the lipid dipole moment and Lennard-Jones (LJ) interactions of polarizable beads are carefully tuned down as a compensation to match, as close as possible, the free energy of partitioning, hydration and vaporization, as depicted in Table 1, using the method outlined by Marrink et al.³⁴. The final dipole parameters for the CNO bead, with an average dipole moment of 8.76 Debye, is $l=0.20$ nm, $q=0.4557$, $\theta=180^\circ$, $k_\theta=4.78$ kcal/mol. For GL1/GL2 bead, with an aver-

age dipole moment of 1.35 Debye, is $l=0.14$ nm, $q=0.175$, $\theta=70^\circ$, $k_\theta=8.40$ kcal/mol. The LJ parameters tuned down from the MARTINI model values corresponding to different chemical species are presented in Table 2. The LJ interaction strengths are divided into nine levels as follows: O) $\epsilon=1.35$ kcal/mol, I) $\epsilon=1.20$ kcal/mol, II) $\epsilon=1.10$ kcal/mol, III) $\epsilon=0.95$ kcal/mol, IV) $\epsilon=0.85$ kcal/mol, V) $\epsilon=0.75$ kcal/mol, VI) $\epsilon=0.65$ kcal/mol, VII) $\epsilon=0.55$ kcal/mol, VIII) $\epsilon=0.50$ kcal/mol. In addition, two hydrophobic interactions, H1-W and H2-W, are also scaled down to 10% to make the lipid model compatible with our protein model³⁶. The peptide model and the lipid model use the same hydrophobic scale. An effective size of $\sigma=0.47$ nm is used for all main CG interaction pairs in the LJ potential.

2.3 Peptide Model

The peptide model parameters were taken from our previous work³⁶, where we capture secondary and super-secondary structure, based on several primary sequences, in peptide folding without any added bias. The bead types of the protein model is largely consistent with the current lipid model, with an addition of a non-polarizable polar side-chain bead type *P*. SVS-1 sequence is mapped to our CG model³⁶ using an hydrophobicity scale⁵. Residues are mapped into polar (*P*), hydrophobic (*H*) and charged (*C*). Valines and prolines are modeled as hydrophobic residues (*H*), with one polarizable backbone bead (*Pol1*), and one hydrophobic side chain bead (*H1*). Lysines are modeled with three beads, a polarizable backbone bead (*Pol1*), a hydrophobic side chain bead (*H1*), and a positively charged second side chain bead (*C+*). Threonine is modeled as a polar residue (*PI*) with one polarizable backbone bead (*Pol1*) and one non-polarizable polar side

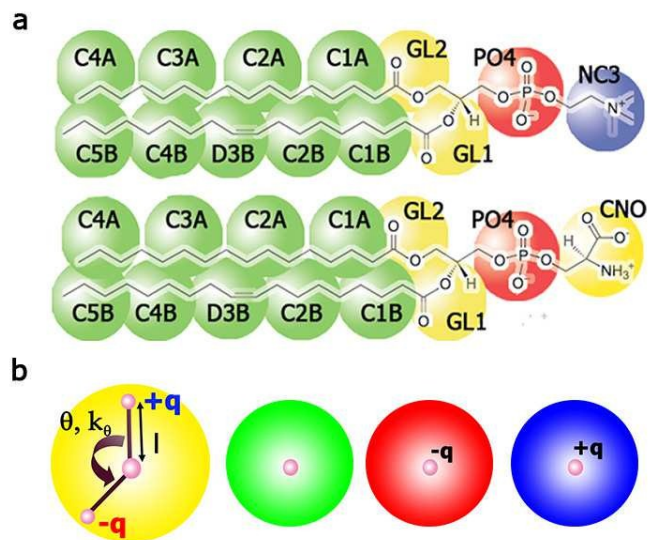


Fig. 1 (a) Mapping scheme for POPC and POPS coarse-grained lipids; colors: green, hydrophobic bead; yellow, polarizable beads; red, negatively charged bead; blue, positively charged bead. (b) Bead types: yellow represents polarizable beads (example: CNO, GL1, GL2), van der Waals radius of the bead encloses positively (+q/P) and negatively (-q/M) charged dummy particles (example: CNP and CNM, G1P and G1M, G2P and G2M respectively). The tunable parameters (l , q , θ , k_θ) are depicted. Blue bead represents a positively charged bead, red bead represents negatively charged bead, and green represents hydrophobic bead.

chain bead (PI). Like the polarizable beads in the lipid model, the backbone coarse-grained bead consists of three interaction sites, the center bead BB and two dipole particles, BBm and BBp . The main site, the center of the BB bead, interacts with other CG beads through a pairwise Lennard-Jones (LJ) potential. Dipole particles BBm and BBp are harmonically bound to the central particle BB (equilibrium distance l , force constant k_l), and carry a positive and negative charge of equal magnitude (q) respectively, as depicted in Figure 1b. These dipole particles interact with other particles via electrostatic interactions. A cosine squared angle potential (equilibrium angle (θ) and angular force constant (k_θ)) was used to control the rotation of BBm and BBp particles. For solvation, the polarizable CG water model was used³⁷. Since the locations of the dipole particles were not fixed, the model is polarizable. That is, changes in dielectric medium or local environment result in induced backbone dipoles and hence structural changes. Details on parameterization methods and force field parameters are provided in Ganesan et al.³⁶. Our model currently does not account for chirality of residues. The peptide model is used with a double well α dihedral potential between backbone beads (force constant of 1.2 kcal/mol) to remove back-

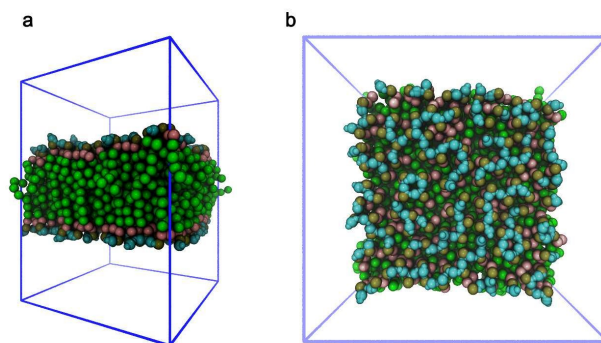


Fig. 2 (a) Side view of POPS bilayer showing the lateral structure of the membrane. (b) Top view of POPS bilayer. Colors: serine (cyan), phosphate (tan), ester (pink), alkyl (green).

ground noise⁴¹

$$U_{dih}(\gamma_{ijkl}) = \cos(3\gamma_{ijkl}) + \cos(\gamma_{ijkl} + 60) \quad (1)$$

$U_{dih}(\gamma_{ijkl})$ has three minima, 60° (right helix) and 180° (sheet) of equal well depth, and -60° (left helix) of a lower depth, and γ_{ijkl} is the dihedral between 4 consecutive backbone beads.

2.4 Simulation Parameters

All simulations are carried out using the GROMACS package version 4.5.4⁴² and visualized using VMD 1.9.1⁴³. The bilayer system is energetically minimized before an isothermal-isobaric (NPT) run, simulation data is collected for 200 ns, of which the last 100 ns is analyzed. Every membrane system studied (atomistic, MARTINI CG or pCG) is made of 240 lipids, 120 on each leaflet. A side view snapshot of POPS bilayer is illustrated in Figure 2a.

In CG bilayer simulations, the Nosé-Hoover^{44,45} thermostat with a time constant of 1 ps is used to maintain a temperature of 300K, and the Parinello-Rahman⁴⁶ barostat with a time constant of 1 ps and an isothermal compressibility of $7.17 \times 10^{-6} (\text{kcal} \cdot \text{mol}^{-1} \text{nm}^{-3})^{-1}$ is used to keep the semi-isotropic pressure at 1 bar in the z direction and 1 bar in the x , y plane. The time step is 5 fs and the neighbor list is updated every 10 steps, for the CG simulations. The long-range electrostatic interactions with periodic boundary conditions (in x , y , z directions) are evaluated using the Particle Mesh Ewald (PME) method⁴⁷ with a global dielectric constant of 2.5. We use the Shift scheme beginning from 0.9 nm and switch the Lennard-Jones interaction to zero at 1.2 nm. The LINCS algorithm⁴⁸ is used for constraining dummy bonds inside polarizable beads.

Table 2 Interaction strength ϵ for LJ interactions (kcal/mol)

Bead (Type)	C0	C+	C-	P1	Pol1	Pol2	W	H1	H2
C0	IV	VII	VII	III	O*	V	II	VII	VI
C+	VII	IV	III	III	O*	II	I	VII	VI
C-	VII	III	IV	III	O*	IV	I	VII	VI
P1	III	III	III	I	I	III*	I	VIII	VI
Pol1	O*	O*	O*	I	I*	I*	I*	VIII	VI
Pol2	V	II	IV	III*	I*	V	IV*	VI	VI
W	II	I	I	I	I*	IV*	III	VIII**	VI**
H1	VII	VII	VII	VIII	VIII	VI	VIII*	IV	IV
H2	VI	VI	VI	VI	VI	VI	VI**	IV	IV

(O: $\epsilon=1.35$ kcal/mol, I: $\epsilon=1.20$ kcal/mol, II: $\epsilon=1.10$ kcal/mol, III: $\epsilon=0.95$ kcal/mol, IV: $\epsilon=0.85$ kcal/mol, V: $\epsilon=0.75$ kcal/mol, VI: $\epsilon=0.65$ kcal/mol, VII: $\epsilon=0.55$ kcal/mol, VIII: $\epsilon=0.50$ kcal/mol)

* 95% of the interaction strength is used to counterbalance the polarization

** 10% of the interaction strength is used to make this model compatible with our protein model³⁶ in hydrophobicity

Simulations with 1M NaCl are performed for both POPS and POPC systems. To make comparisons with MARTINI force field, all 4 systems (POPC without NaCl, POPS without NaCl, POPC with 1M NaCl, and POPS with 1M NaCl) are simulated using both our pCG model as well as the MARTINI force field. The simulation setups used for pCG and MARTINI simulations are mostly identical. The only difference is the increase in time step with MARTINI force field (20 fs). This was done to maintain consistency. Explicit MARTINI polarizable water model is used for both pCG and MARTINI simulations^{34,37}. We also compared simulation performance between MARTINI force field and pCG, with polarizable water and POPC lipids (240 POPC lipids and 7757 water particles). For this comparison analysis, MARTINI parameters were borrowed directly from their study^{34,37}, while parameters detailed above were used for pCG. We found MARTINI simulations to be twice as fast as our model.

Simulations with the peptide are performed with 240 lipids of polarizable POPS, polarizable POPC, POPS without dipoles, and in water. For systems with the peptide and the bilayer, a random conformation of the peptide is introduced 5nm away from a self assembled bilayer. Counterions are added to neutralize the system. The peptide is constrained and a 10 ns NPT simulation is performed to allow the counterions to equilibrate. Constrains are removed to collect 300 ns NPT data, all of which are analyzed. For better sampling, we run 9 randomly constructed simulations of each pCG POPS system, and 6 runs for pCG POPC, POPS without dipoles (POPSnd), and in water. An image of the bilayer-peptide system setup is shown in Figure S1.

Atomistic POPS and POPC bilayer simulations are per-

formed with GROMOS 53A6 lipid force field⁴⁹. The thermostat coupling method, velocity rescaling with a stochastic term (v-rescale), with a time constant of 0.1 ps is used to maintain a temperature of 300K. The Parinello-Rahman barostat with a time constant of 5.0 ps and isothermal compressibility $1.08 \times 10^{-5} (\text{kcal} \cdot \text{mol}^{-1} \cdot \text{nm}^{-3})^{-1}$ are used to maintain semi-isotropic pressure at 1 bar in the z direction and 1 bar in the x, y plane. The time step for dynamics is 2 fs and the neighbor list is updated every 5 steps. Long-range electrostatic interactions with periodic boundary conditions (in x, y, z directions) are evaluated using the PME method.

2.5 Analysis Methods

2.5.1 Calculation of Standard Errors

The estimation of the standard error for the average of the property X, is calculated by block average. Namely, the whole trajectory is divided into N blocks, each with M frames. The average of X for each block, and standard deviation from block averages is calculated. The standard error is the standard deviation over \sqrt{N} . To ensure the property X is independent in each M-sized block, we calculate the normalized time correlation function of the fluctuations for X,

$$C(t) = \frac{\langle \delta X(0) \delta X(t) \rangle}{\langle \delta X(0) \delta X(0) \rangle} = \frac{\langle \delta X(0) \delta X(t) \rangle}{\delta X^2} \quad (2)$$

where $\delta X(t) = X(t) - \langle X \rangle$, and $\langle \delta X^2 \rangle$ is the mean squared fluctuation. The size M is set to equal twice the correlation time $\tau_X = \int_0^\infty C(t) dt$. The standard error in X can also be directly obtained from:

$$se[X] = \sqrt{\frac{2\tau_X}{T_{run}}} < \delta X^2 >^{1/2} \quad (3)$$

All standard error calculated in this paper use the block average method.

2.5.2 Density Distribution

In the CG bilayer system, the density distribution for each bead in the lipid is plotted along the bilayer normal direction. In atomistic simulations, instead of using the position of each atom, center of mass of several atoms corresponding to each CG bead is evaluated for better and more direct comparison to CG data. The scheme for atoms mapped to beads is shown in Figure 1a.

2.5.3 Susceptibility Profile

The bilayer is divided into several slabs of 5\AA , in the axial direction, starting from the center of mass of the bilayer. Then the susceptibility or specific dielectric constant of each slab in a direction parallel to the membrane interface is calculated using the following equation based on linear response theory⁵⁰,

$$\chi_{//}\epsilon_0 = \beta \frac{\langle |\Delta \mathbf{M}_{//}|^2 \rangle}{\langle V \rangle} = \beta \langle |\Delta \mathbf{P}_{//}|^2 \rangle \langle V \rangle \quad (4)$$

where $\mathbf{M}_{//}$ and $\mathbf{P}_{//}$ are the total dipole moment and polarization density in the direction parallel to the bilayer, and the Δ indicates the difference between the value in each sample and the time-averaged one. ϵ_0 is the dielectric constant of vacuum, V is the slab volume and $\beta = 1/k_B T$. Ergodicity is assumed for time averages in the equation. To investigate the effect of polarization on bilayer dielectric profile, only polarizable beads, including serine, ester groups and water molecules in CG simulation, and their corresponding atom groups in atomistic simulation are taken into consideration. The dipole moment of the polarizable CG beads is assigned to their central main site and the dipole moment of atom group is assigned to their center of mass.

2.5.4 Line Tension

Line tension of POPC and POPS bilayer is computed from a ribbon structure in the z direction. Initial and final conformations are shown in Figure S2. Ribbon structure is simulated using a $NP_{xy}L_zT$ ensemble and evaluated using Eq.(5)⁵¹.

$$\Lambda = \frac{1}{2} \left\langle L_x L_y \left[\frac{P_{xx} + P_{yy}}{2} - P_{zz} \right] \right\rangle \quad (5)$$

where L_x , L_y are the sizes of the simulation box in x and y axis, and P_{xx} , P_{yy} and P_{zz} are the diagonal elements of pressure tensors along x , y , z axis.

2.5.5 Bilayer Potential

Electrostatic potential of the bilayer across the box is calculated using the `g.potential` program in the GROMACS 4.5 package⁴². It is computed by evaluating the double integral of the charge density ($\rho(z)$):

$$\psi(z) = -\frac{1}{\epsilon_0} \int_{-\infty}^z dz' \int_{-\infty}^{z'} \rho(z'') dz'' - \frac{z}{\epsilon_0 L} \int_0^L \rho(z') z' dz' \quad (6)$$

where ψ is the electrostatic potential and ϵ_0 is the dielectric constant of vacuum. L is the length of simulation box in the bilayer normal direction. Periodic boundary condition is assumed in the second term, *i.e.* $\psi(0) = \psi(L)$.

2.5.6 Cluster Analysis

To characterize the clustering of head groups in lipid bilayers, a distance-based clustering method is adopted. For the pCG model, neighboring lipids that have dummy particles with opposite charges residing within a cutoff distance are considered connected, and all lipids that are connected through dipolar connections are classified as a cluster. Dipolar connections are defined based on contact distance between a positively

charged and a negatively charged dummy particle in close contact with each other. The cutoff distance used to determine a dipolar connection is based on pairwise radial distribution functions (RDF) between lipid beads with opposite dummy charges, as shown in Figure S3a and Figure S3b. The position of the RDF first peak, from positively charged CNO dummy beads to all negatively charged particles (CNM, PO4, G1M, G2M) is used to define the cutoff distances. These distances are 3.0Å for CNP-CNM pair (serine-serine), 4.2Å for CNP-PO4 pair (serine-phosphate), 3.5Å for CNP-G1M pair (serine-ester), and 4.5Å for CNP-G2M pair (serine-ester). If either of these distances are satisfied between two lipids, they are considered to be interacting lipids forming a dipolar connection.

The original MARTINI CG model does not have dipolar particles, therefore an additional distance, based on main CG bead sites, are defined to compare pCG and MARTINI model directly. From the defined interacting lipids, pairwise distance cutoffs of 6.1Å for CNO-CNO pair and 5.5Å for CNO-PO4 pair are defined. These are obtained by including the first peak of respective radial distribution functions (results not shown). Between any two lipids, if both cutoff distances are satisfied, they are considered to be adjacent to each other. An adjacency matrix with $N \times N$ elements, where N is the number of lipids in the system, is introduced to characterize the dipolar connectivity between all lipid pairs, in the following form:

$$\underline{\underline{\mathbf{A}}} = \{a_{ij}\} = \begin{cases} 1 & \text{if } \mathbf{r}_i^{\text{CNO}} - \mathbf{r}_j^{\text{CNO}} \leq 6.1\text{\AA} \\ 1 & \text{else if } \mathbf{r}_i^{\text{CNO}} - \mathbf{r}_j^{\text{PO4}} \leq 5.5\text{\AA} \\ 0 & \text{otherwise} \end{cases} \quad (7)$$

where the superscript for the position vector \mathbf{r} denotes the bead type concerned, the subscript is the lipid index, which is a number assigned from 1 to N . With this matrix, the classification of physically neighboring lipid clusters is transformed to a connected-components labeling problem. The `NetworkX 1.6` module in `Python 2.7` is used to perform a connected-components labeling analysis and classify connected lipids in the bilayer as clusters⁵².

As for atomistic simulations a cutoff distance of 3.5Å between hydrogen and oxygen atoms is used, which is the typical hydrogen bonding distance⁵³. The adjacency matrix for the all-atom data is defined below:

$$\underline{\underline{\mathbf{A}}} = \{a_{ij}\} = \begin{cases} 1 & \text{if } \min\{\|\mathbf{r}_i^{\text{H}} - \mathbf{r}_j^{\text{O}}\|\} \leq 3.5\text{\AA} \\ 0 & \text{otherwise} \end{cases} \quad (8)$$

The superscript for the position vector \mathbf{r} in Eq.8 denotes the atom type (H for hydrogen and O for oxygen) and the subscript denotes the lipid index. Whenever there is at least one pairwise distance between oxygen and hydrogen in two differ-

ent lipids that is within 3.5\AA , a hydrogen bond is considered formed between the two.

2.5.7 Ion Bridge Connectivity

The first peak of the RDFs between a positively charged ion (Na^+) and other negatively charged beads in a lipid is shown in Figure S3c and Figure S3d, and is used to define cut-offs for ion-bead interactions (CNM: 4.4\AA , PO4: 6.1\AA and G1M/G2M: 5.1\AA). In other words, an ion is bound to a lipid if the distance between the positively charged ion and the negatively charged lipid particle is less than the cutoff distance. An ion bridge is formed when one lipid connects to another lipid via an ion-lipid connection.

3 Results and Discussion

3.1 Structural and Dynamic Membrane Properties

Bilayer Self-Assembly: Snapshots of the bilayer self-assembly process are shown in Figure S4 for POPS, and Figure S5 for POPC. In both systems, the lipids begin aggregating in less than one nanosecond and form a single disordered aggregate. As system evolves, the aggregate rearranges to form a defect-free bilayer in less than 12 ns.

Area per Lipid and Bilayer Thickness: The bilayer area per lipid at different NaCl concentrations is shown in Figure 3. The area per lipid of POPS and POPC at 0M ion concentrations (i.e. with only counterions) is 65\AA^2 , for both systems with MARTINI force field³⁴, and 62\AA^2 and 60\AA^2 respectively with our polarizable model. The standard errors, determined from block averages, are within 10^{-3}nm^2 for all the four systems. One major distinction in our results compared to the MARTINI force field is the ability of our model to capture a difference between the area per lipid of POPC and POPS. Due to the absence of any dipolar interactions, the area per lipid values of POPC and POPS bilayer are nearly identical in MARTINI. A condensation effect is observed in pCG POPS bilayer induced by strong dipolar interactions between the serine headgroups. In experiment, the area per lipid of POPS has been reported by different groups to be $45\text{-}55\text{\AA}^2$ ^{54,55} whereas for POPC it is around $62\text{-}68\text{\AA}^2$ ⁵⁶⁻⁵⁹. Even though our POPC area per lipid (62\AA^2) is about 3\AA^2 lower than that of MARTINI POPC (65\AA^2), both coarse grained values are within reasonable range, in comparison to both experiments and all-atom simulations⁶⁰.

In both MARTINI and our pCG model, the decrease in area per lipid induced by the addition of 1M NaCl is in agreement with previous all-atom simulations¹⁸, and experimental measurements⁶¹ using various lipid bilayers. All-atom study by Pandit et al. characterizing the effect of NaCl on DPPC bilayers, showed that the area per lipid of the bilayer decreases with the presence of ions²². The reduction in area per lipid is due to a condensation effect induced by Na^+ ions. On the other

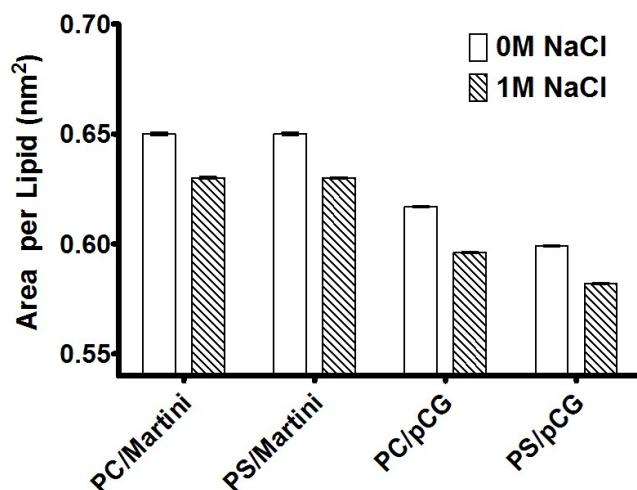


Fig. 3 Area per lipid change induced by the addition of 1M NaCl. The standard error of mean is within 10^{-3}nm^2 .

hand, Tieleman's study on atomistic POPS with GROMOS, in the presence of ions does not show a marked effect on area per lipid²⁴. Our model, along with MARTINI shows a 3-4% decrease in area per lipid with the presence of monovalent ions, in both POPC and POPS systems.

The average bilayer thickness is listed in Table SI. Bilayer thickness is measured as the distance between vertical positions (z-axis) of phosphate groups on either leaflet. The bilayer thickness of pCG POPS is smaller than that of pCG POPC by $\sim 0.5\text{\AA}$. In all-atom and experimental studies, the bilayer thickness of POPS is reported to be 38.2\AA and for POPC it is 39.1\AA ^{20,56}, which shows the same trend. In addition, with the presence of ions, all-atom simulation data with POPC, and POPC-POPS mixed systems, show an increase in bilayer thickness, which is in agreement with our bilayer thickness increase of 0.7\AA ^{61,62}. The change in bilayer thickness is attributed to an increase in head group interaction with ions and the decrease of area per lipid.

Density Distribution: Density distributions (see Figure 4) of different head groups of POPC and POPS were evaluated to estimate the effect of added dipolar particles. As shown in Figure 4b and Figure 4d, the regions occupied by phosphate (PO4) and serine groups (CNO) in POPS overlap in space for our model and all-atom data. This effect is primarily due to the electrostatic interactions among the serine and phosphate groups, between lipids and within lipids, that causes the phosphates to lie in the same vertical position (z-axis) as the serine groups. That is, with the addition of head group dipoles, both the phosphate and serine groups lie on the same plane. However, with the MARTINI force field the serine head group bead is located above the phosphate bead, as seen by the out-

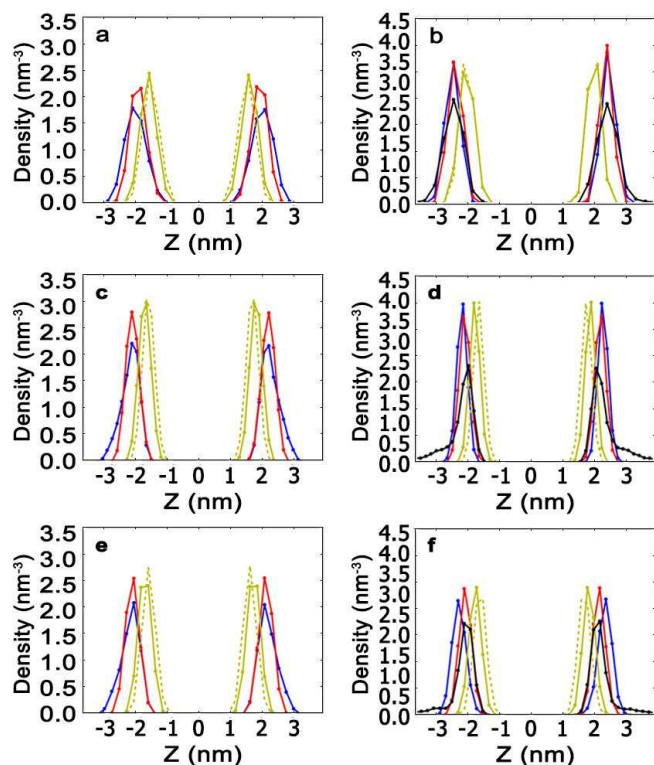


Fig. 4 Density distribution of (a) POPC from all-atom data, (b) POPS from all-atom data, (c) POPC from pCG data, (d) POPS from pCG data, (e) POPC from MARTINI data, (f) POPS from MARTINI data. Solid yellow: GL1; dashed yellow: GL2; red: PO4; blue: NC3/CNO; black: Na⁺.

ward shift of the PO4 and CNO distribution peaks (Figure 4f). This is due to a lack of any dipole-dipole or electrostatic interactions between CNO-CNO beads and CNO-PO4 beads in MARTINI leading to an increase in conformational freedom of CNO-PO4 beads.

For the 1M NaCl system, both pCG POPS and pCG POPC exhibit Na⁺ ion penetration as observed by the increase of the Na⁺ density distribution near the head group region (black curve in Figure S6a and Figure S6b). There is a clear distinction between pCG POPC and pCG POPS, a deeper ion penetration in the PS system is observed. Due to this effect, some of the charges on phosphate beads are satisfied, and the serine bead is seen to interact less with the phosphate group, and more with ions and water. This can be better understood by comparing serine and phosphate positions in Figure S6b and Figure 4d. By the addition of NaCl the CNO peak shifts outwards, towards the solvent. The ion density curves with both our model and MARTINI (black curve in Figure S6a and Figure S6b) is similar in location to the Na⁺ ion peak with old CHARMM parameters, where Na⁺ over bind-

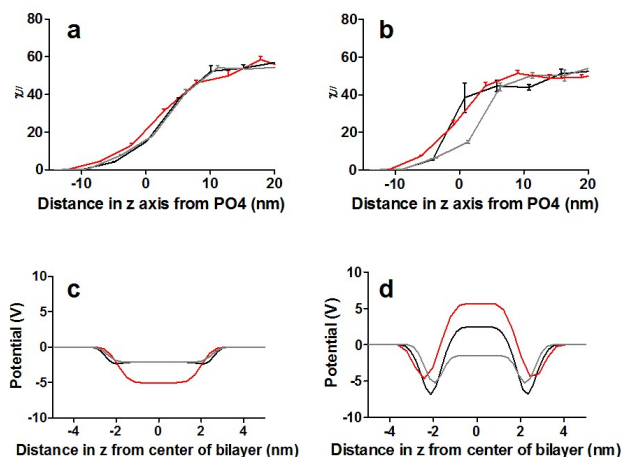


Fig. 5 Susceptibility profile of (a) POPC and (b) POPS bilayers. Potential profile of (c) POPC and (d) POPS bilayer. Atomistic profile is represented in red, MARTINI in gray and pCG in black.

ing was observed⁶³. In order to characterize the ion exchange between membrane and solution environments, we looked at ion residency time (τ) using the method outlined by Sachs et.al.²¹. The ion residency time of our CG ion (Figure S7) is more than an order of magnitude less than that of all-atom ions using GROMOS (Figure S8), OPLS forcefield²¹ and new CHARMM parameters⁶³; thus suggesting that our ions are not stuck to the lipid bilayer. However, we would like to point out that the monovalent ion used in this study, both with MARTINI and pCG forcefields, is just a prototype monovalent ion, any type of monovalent cation is modeled with the same parameters; and all beads in the model have the same size.

Susceptibility Profile and Dielectric Potential: Susceptibility (χ) is a measure of dipole moment sensitivity to changes in external electric field. Both water molecules and head group beads contribute to this dipole moment, and hence χ . Dielectric susceptibility of a bilayer-water system with atomistic force field GROMOS (red curves), our polarizable CG model (black curves) and the MARTINI force field (gray curves) for POPC and POPS is depicted in Figure 5a and 5b respectively.

In the case of POPC (Figure 5a) there is a gradual gradient in χ from the center of the bilayer (x axis <0) to bulk water (x axis >0). This trend is consistent in all three systems. However, in the case of POPS (Figure 5b), the regions near the head groups (interfacial region) have a high dielectric contribution in both all atom simulations (red curve) as well as with pCG (black curve). This effect is not captured in MARTINI (gray curve) largely due to the lack of head group bead polarizability. A CARS (Coherent Anti-Stokes Raman scattering) microscopy experiment used by Cheng et al. show that interfacial water molecules near POPS multilamellar vesicle is

more polarized than those near POPC multilamellar vesicle⁶⁴, which can be interpreted as being consistent with our finding that PS interfacial dipoles are more prone to the change of external electric field.

To investigate the effect of bead polarization on membrane electrostatics, we computed transmembrane electrical dipole potential (V) that arises solely from POPC and POPS lipid bilayers, excluding water molecules and ions. Transmembrane potential for POPC and POPS bilayer systems with atomistic force field GROMOS (red curves), our polarizable CG model (black curves) and the MARTINI force field (gray curves) is depicted in Figure 5c and 5d respectively. This potential largely arises from the alignment of lipid dipole head groups. For the POPC bilayer, the dipole potential evaluated using pCG and MARTINI is nearly indistinguishable, with the exception of a marginal decrease in potential is observed at the interfacial region with pCG, owing to the presence of polarizable ester groups. This result is in disagreement with the observations from Orsi et al., which found that ester groups of PC membranes play a more significant role in electrostatic potential⁶⁵.

In the case of POPS, there is a more significant gradient in dipole potential change from the interfacial region to the hydrocarbon core (see Figure 5d, from $x=0$ to $|x|=2$), with pCG and all atom bilayers. Although the absolute value of the dipole potential at the center of the bilayer is around +2.5V with pCG, and +5V with the atomistic model, we are able to capture the right trend. That is, MARTINI yields a negative potential at the center of the bilayer, whereas, pCG and atomistic yield a positive potential.

PS Cluster: The presence of lipid clusters in PS and mixed PC/PS bilayers has been observed in the atomistic simulations^{24,62}. Since the head group of POPS in our model is capable of forming dipole-dipole interactions, dynamic clusters are observed on the membrane surface see Figure 6b and Figure 2b). That is, there are dipolar interactions connecting oppositely charged dummy particles of neighboring lipids. As shown in Figure 6d, on average, there are around 30 clusters in our polarizable lipid CG model, and around 20 clusters in POPS all-atom model. The clusters in our CG model are mostly linear whereas in all-atom simulations they have more branches. This is because, the serine group in the all-atom system can form multiple hydrogen bonds between lipids, while the serine CG bead can only form two dipolar connections. All clusters observed in the simulations are dynamic in nature, they emerge and disappear. Therefore, these dipolar interactions observed in our CG model mimic the hydrogen bonding network observed in all atom bilayers⁶⁶ (Figure 6a). These clusters are not present in the MARTINI POPS system (Figure 6d), due to the inability of the model to capture dipolar interactions. Clearly, pCG is capable of reproducing the essence of cluster formation, which is a distinct property of POPS lipids.

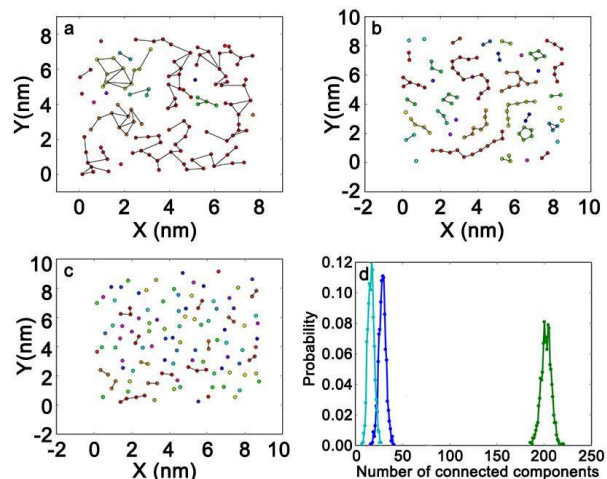


Fig. 6 Top view of head group clusters for a leaflet (each point represents a phosphate atom, and lines represents lipid connectivity) in (a) all-atom POPS bilayer, (b) pCG POPS bilayer, and (c) MARTINI POPS bilayer. Distinct colors are used to distinguish individual clusters. (d) Probability distribution of number of clusters in POPS bilayer in all-atom (cyan), pCG (blue), and MARTINI (green) systems.

The dipoles in polar beads, act as pseudo hydrogen bonds and assist in the interactions between head groups. These head group interactions lead to the formation of clusters. To confirm that our clusters are dynamic, and often break and reform, we performed a cluster life time analysis (see Supplementary material, section: Dipolar Cluster Half-Life). From our analysis it is clear that the clusters are dynamic, and often exchange lipids.

Line tension: Our model predicts a line tension of 37.3 ± 4 pN for POPC bilayer. This value is within the range of that predicted for similar lipids like DOPC and SOPC ($6 \sim 25$ pN)^{51,67,68}. Thus the model can capture the right barrier in pore formation of POPC bilayers, and the presence of dipolar particles does not significantly increase this energetic penalty or the barrier for pore formation. The line tension for pCG POPS is 51.7 ± 5 pN. The time scale for edge reconstruction with pCG POPS was significantly higher than that with pCG POPC. The higher line tension with pCG POPS indicates a higher energy barrier for pore formation in lipid bilayers, which is expected due to stronger head group interactions between lipids.

Ion Bridges: To better characterize ion bound lipids, we classified lipids bound to ions via ion bridges, where an ion bridge is defined as an ion connecting two lipid molecules based on cut-off distances (see Methods section). For the POPS bilayer system with 0M NaCl (i.e. with counterions), 20% of lipids are bound to only one ion bridge, 49% to two

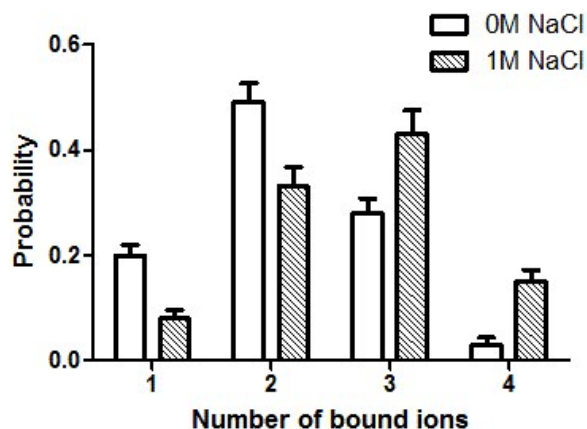


Fig. 7 Probability of 1,2,3 and 4 ion bridges bound to a POPS lipid at different ion concentrations.

ion bridges, 28% to three ion bridges and almost none of the lipids are bound to four ion bridges (Figure 7). However, when 1M NaCl is added to the system, the number of 3 and 4 ion bridges bound to a lipid increases significantly to, 43% and 15% respectively. This suggests that the addition of extra ions to the system connects more lipids, forming larger ion-mediated lipid regions. This result is consistent with many all-atom studies on anionic bilayers^{18,24,61}.

3.2 Membrane-Induced SVS-1 Folding

The presence of dipole particles in lipids (POPS) and peptide (SVS-1) enabled us to better investigate the role of electrostatic interactions. Figure 8 includes 4 snapshots of one representative run of SVS-1 peptide with pCG POPS bilayer. Within the first 10 ns, lysine side chains of the peptide (brown) are attracted to the anionic bilayer. Once the side chain charges are satisfied, the dipoles of the backbone beads interact with each other, which aid in formation of a β -hairpin within 30 ns in most trials. The peptide is dynamic on the surface of the bilayer and explores different registers.

This is consistent with experimental behavior of SVS-1, which has been shown to preferentially adopt a β -sheet conformation both in the presence of anionic membranes and tumor cells^{8,38}. To characterize the lateral position of the peptide, we looked at z distance between side chain beads of each of the β strand residue, and phosphate layer, with time. Figure S9 represents this z distance (scale on the color bar) for one representative trial that folds into a β -hairpin. Initially, the lysine distances from the phosphate layer are lower than the valines (dark blue in Figure S9a, $<2\text{\AA}$), however, with time the valine distances from the phosphate layer become more negative (green and blue, -4 to -7\AA). Negative distances in Figure

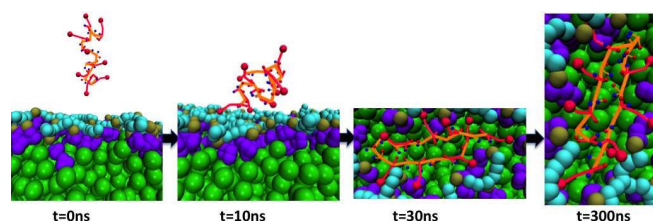


Fig. 8 Stages in SVS-1 sheet formation: peptide is randomly placed above the bilayer at $t=0\text{ns}$; lysine side chains interact with anionic POPS within a few ns. With lysine side chains buried in the bilayer, the backbone dummies interact to form sheets, which are formed as early as 30 ns in some runs. The peptide is dynamic on the surface of the bilayer and largely retains sheet content by the end of 300 ns. Colors: lipid hydrophobic core (green), peptide backbone (orange), positive and negative dummies in blue and red, phosphates in tan, esters in purple, CNO in cyan and lysines in crimson.

S9 denote deeper penetration beneath the phosphate layer. That is, with time the valines face the hydrophobic phase to interact with the alkyl beads, while the lysines continue to interact with the head group region (PO4 and CNO). This leads to a more negative distance for valines than lysines in Figure S9.

A total of 9 trials were performed to validate the significance of our results. Details of 3 random trials are shown in Figure 9. Figures 9a-c depicts in-register sheet fraction (Fr_{sheet})³⁶, center of mass distance (com) of the peptide from the bilayer (Δz), and end to end distance of the peptide (L_c), respectively. Different colors represent different trials. Another 6 random trials are shown in Figure S10. In total, 5 out of 9 runs folded into stable, sheet-like conformations. From Figure 9a and 9b, as the peptide reaches the bilayer (denoted by 20\AA on the y axis), the in-register sheet fraction gradually increases, suggesting the involvement of the bilayer in driving peptide folding. It is important to note that the peptide is dynamic on the bilayer, which can be seen by fluctuations in in-register sheet fraction, which is a strict measurement of sheet contacts. In addition to β -hairpin, off-register conformations are observed, as depicted by the representative peptide conformations with in-register sheet fraction between 0-0.2, 0.2-0.4, 0.4-0.6, 0.6-0.8 and 0.8 to 1 in Figures 9e, 9d, 9g, 9f and 9h respectively. Conformations with $Fr_{sheet} > 0.5$ are largely sheet-like. Time evolution of L_c of the peptide is shown in Figure 9c, a decrease in L_c as the peptide reaches the bilayer and adopts a sheet-like conformation is observed. The trend in L_c correlates with the pair fraction (Figure 9a). That is, with an increase in Fr_{sheet} there is a decrease in L_c .

However, not all trials lead to sheet-like conformations (blue curves in Figure 9). The peptide is dynamic and folds and unfolds on the surface of the bilayer. For example, in Figure S10e there are 27 transitions from folded ($Fr_{sheet} > 0.7$) to

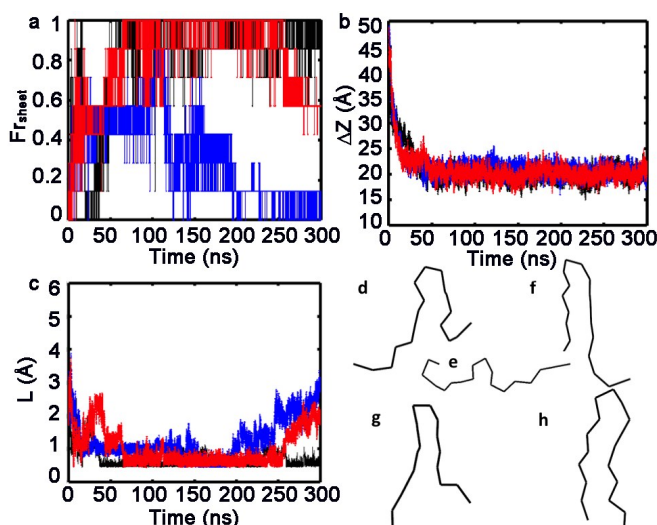


Fig. 9 Time evolution of (a) sheet pair fraction (Fr_{sheet}) of the peptide; (b) center of mass (com) distance of the peptide from the phosphate beads on the bilayer (Δz); (c) end to end distance (L_c) of the peptide, evaluated between the first and the last backbone bead. Each color represents a single run. Representative snapshots of conformations explored, each with a in-register sheet fraction of (d) 0.28, (e) 0.14, (f) 0.71, (g) 0.57 and (h) 1.0. All data from our polarizable coarse-grained models.

the unfolded state ($Fr_{sheet} < 0.3$) in 300ns.

Figure S10a-f depict Δz , and Fr_{sheet} of multiple trials. Even though a small double well dihedral bias for both helical and sheet conformations is added to the force field, no helicity was observed for the SVS-1 peptide with pCG POPS at the interface. This is not surprising as the peptide has a distinct sheet pattern of alternating cationic and hydrophobic residues, along with a designated turn region⁶⁹.

As control systems, simulations of (a) pCG SVS-1 and pCG POPC bilayer, (b) pCG SVS-1 and POPS bilayer without polarizable particles (POPSnd *i.e.* POPS no-dipole), and (c) pCG SVS-1 in water were analyzed. Figures S9a and S9d, S9b and S9e and S9c and S9f, depict Fr_{sheet} , Δz , and L_c of runs with pCG SVS-1 and pCG POPC, and pCG SVS-1 and POPSnd (or POPS no dipole), respectively. Each color in the Figures represents an individual trial, a total of 6 distinct runs are represented. Fr_{sheet} explored by these systems is largely below 0.3 and L_c , above 20Å. Therefore, there is a lack of secondary structure content in these systems, and a preference for more extended conformations with L_c ranging from 20 to 50Å (see Figure S11c and S11f). Any sheet-like conformation explored in the case of pCG POPC (red and magenta lines in Figure S11a) are structures explored by the peptide in water. This is supported by the Δz plot (Figure S11b), which shows that the distance between the peptide and the com of the bilayer is greater than 35Å until 30-40 ns. A time-lag in peptide-pCG

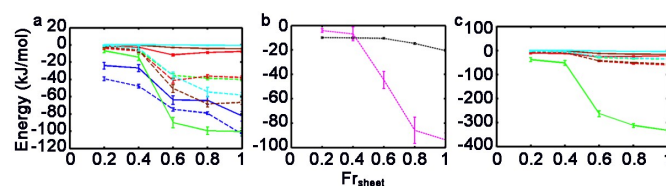


Fig. 10 LJ pairwise (dashed lines) and Coulombic energies (solid lines) as a function of Fr_{sheet} for (a) PO4-BB (green), CNO-BB (red) and BB-BB (blue), GL2-BB (cyan), GL1-BB (brown); (b) hydrophobic side chain self interaction (black) and hydrophobic side chain-alkyl (magenta); (c) PO4- SC_{C+} (green) and CNO- SC_{C+} (red), GL2- SC_{C+} (cyan), GL1- SC_{C+} (brown). Data from pCG POPS bilayer system.

POPC bilayer binding is observed by comparing the time evolution of Δz in Figures S9b, S9e, and 9b. That is, there is a noticeable time difference of about 10ns between peptide interaction with pCG POPC, in comparison with POPS with and without dipoles. Therefore, the serine dipoles might not play a significant role in attracting the peptide to the bilayer surface.

Time evolution of sheet content, end to end distance, average peptide dihedral, and H1 distance (i to $i + 4$ backbone distance)³⁶ of pCG SVS-1 in water are shown in Figure S12a-d respectively. SVS-1 explores unfolded, helical (average dihedral angle of 40-60° and H1 distance of 5-7Å) and sheet-like conformations (sheet contact greater than 0.7 and L_c within 1-2 nm) without exhibiting a preferred structure or stable state(s) in water. From these four plots, we conclude that SVS-1 is intrinsically disordered in water. This is consistent with both experimental data and the design strategy, *i.e.* SVS-1 was designed to remain disordered and inactive in aqueous solution⁸. In fact, most linear AMPs are not structured in solution, and the induction of secondary structure on membrane surfaces is known to enhance amphipathicity, which plays a key role in the antimicrobial function of these peptides⁷⁰. This also means that the peptide could be collapsed before interacting with the bilayer. However, the fact that a stable β -sheet conformation is observed, only on SVS-1 interaction with pCG POPS and not otherwise, reinforces the role of pCG POPS in stabilizing β -sheet conformations in SVS-1 peptide.

These results, albeit expected, raise a series of important questions, (a) what drives the folding of pCG SVS-1 on pCG POPS bilayers?, (b) what is the role of dipoles, both in the peptide and the membrane? (c) why does the peptide not fold on pCG POPC and POPSnd (POPS without dipoles) bilayers, and finally, (d) how do the side chains influence the folding process? To answer these questions, we turned to energetic contributions.

Figure 10a represents distinct energetic contributions between the CNO beads and the peptide backbone beads (BB) (red curves), phosphate-BB (green curves), GL1-BB (brown),

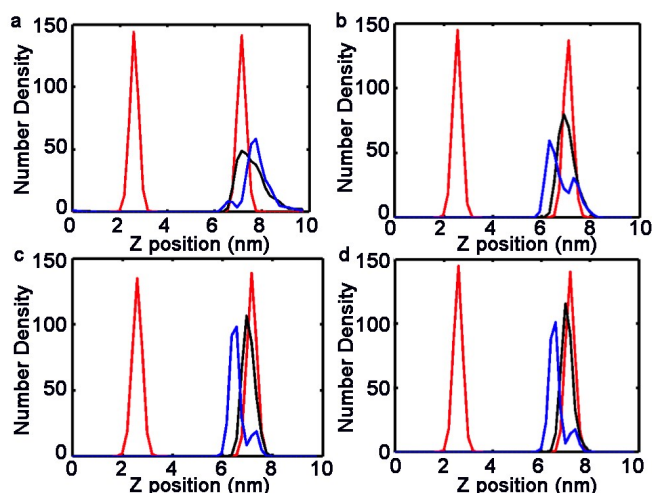


Fig. 11 Number density distribution of PO4 (red curves), lysine side chain (SC_{C+}) (black curves) and valine side chain beads (blue curves) over a time period of (a) 0-25 ns, (b) 25-50 ns, (c) 50-75 ns and (d) 75-100 ns. Side chain distributions are scaled by a factor of 5 for easy comparison.

GL2-BB (cyan) and between backbone beads themselves (blue curves). All five interactions display a swift decrease in energy from the unfolded state (Fr_{sheet} around 0.2) to the folded state ($Fr_{sheet} > 0.6$), thus denoting a cooperative transition in folding. Figure S14 shows an example of a BB-BB dipole interaction (purple box) and an example of CNO-BB dipole interaction (blue box), where the backbone dipole vectors are represented in brown and the head group dipole vectors in green. Cooperativity in BB interaction is expected and consistent with our previous study³⁶, however, the interaction of BB with PO4 and CNO beads also display similar trends. This is because, sheet formation in SVS-1 is not just driven by dipolar contacts within the sheet, but also stabilized by interactions between the bilayer headgroups and the peptide. This result stresses on the relevance of the “polarity profile” of bilayers, or the gradient in electrical polarity due to chemical heterogeneities at membrane interfaces. It has been speculated by White’s group, among others, that the chemical heterogeneities of the interface will provide possibilities for non-covalent, stabilizing interactions with peptides^{5,71}. Both GL1- SC_{C+} (brown) and GL2- SC_{C+} (cyan) interactions seem to be the least significant, with LJ interactions (dashed brown and cyan curves) a little more pronounced than Coulombic interactions. This is largely due to the positioning of the peptide in the bilayer, which is below the PO4 layer as evident from Figure S9.

Figure 10b represents pairwise energies of valine-valine beads (black dashed curve) and valine-lipid alkyl tails (magenta dashed curve). Both these terms show clear coopera-

tive trends of lower energy for the folded state. However, a sharper transition between the folded and unfolded states is observed in the case of valine-alkyl interactions. To understand the interplay between the lysine (SC_{C+})-phosphate and valine-alkyl interactions, we looked at density distributions of lysine and valine side chains of a representative run (black and blue curves in Figure 11, respectively) at different time periods. Density distributions of phosphates on both leaflets (red curves in Figure 11) are shown in red, to denote the bilayer boundaries. Figure 11 shows the distribution from (a) 0-25 ns, (b) 25-50 ns, (c) 50-75 ns and (d) 75-100 ns. As can be seen from these plots, lysine insertion into the phosphate region is the first crucial step (black curve in Figure 11a). With time, the valine side chains flip towards the interior of the bilayer. By 75 ns, almost all the valine side chain beads are completely buried in the hydrophobic region (Figure 11c). Another trajectory is represented in Figure S13, which also shows similar trends in lysine and valine side chain insertion, *i.e.* by 75ns, the hydrophobic side chains are buried in the membrane. These results reinforce the importance of amphiphilicity in membrane-induced folding of AMPs.

Figure 10c represents distinct energetic contributions between the bilayer and charged lysine side chain beads (SC_{C+}), along the reaction coordinate Fr_{sheet} . Green curves correspond to interaction between phosphate beads and SC_{C+} , red curves correspond to interaction between CNO beads and SC_{C+} , brown curves correspond to interaction between GL1 beads and SC_{C+} and cyan curves correspond to interaction between GL2 beads and SC_{C+} . All solid lines are Coulombic contributions and dashed lines, LJ interactions. Phosphate- SC_{C+} Coulombic interaction (green solid curve) displays a sharp transition from the unfolded state (Fr_{sheet} around 0.2) to the folded state ($Fr_{sheet} > 0.6$). A similar transition of much lower magnitude is observed in the case of CNO- SC_{C+} interaction. Again, both GL1- SC_{C+} (brown) and GL2- SC_{C+} (cyan) interactions seem to be the least significant, with LJ interactions (dashed brown and cyan curves) a little more pronounced than Coulombic interactions, due to the location of the peptide. Thus, phosphates play a larger role in interaction with cationic side chains. This result can be reconciled with Figure 8 and 11, where the lysines are seen to drive the peptide towards the bilayer. Positioning of lysine residues to interact with lipid phosphates is a property of many cationic AMPs like CM15, a lysine enriched cecropin-melittin hybrid⁷².

SVS-1 does not fold with pCG POPC and POPSnd bilayers, energetic contributions with respect to L_c , of one representative trajectory (brown curves) is depicted in Figure 12. Figures 12a-c correspond to POPSnd and Figure 12d-f to pCG POPC. Figure 12a and 12d represent energetic contributions between the head group beads (CNO for POPSnd and NC3 for POPC) and the peptide backbone beads (BB) (red curves), phosphate-BB (green curves), GL1-BB (brown),

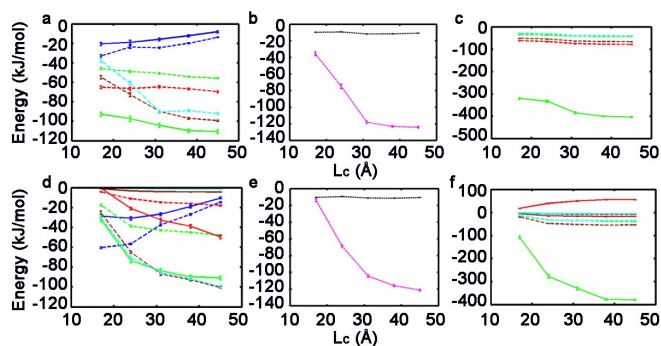


Fig. 12 LJ pairwise (dashed lines) and Coulombic energies (solid lines) as a function of L_c for (a and d) PO4-BB (green), CNO-BB (red) and BB-BB (blue), GL2-BB (cyan), GL1-BB (brown); (b and e) hydrophobic side chain self interaction (black) and hydrophobic side chain-alkyl (magenta); (c and f) PO4- SC_{C+} (green) and CNO- SC_{C+} (red), GL2- SC_{C+} (cyan), GL1- SC_{C+} (brown). Data for POPS bilayer without dipole particles represented on top (a, b, and c), and pCG POPC bilayer-SVS-1 system below (d, e and f).

GL2-BB (cyan) and between backbone beads themselves (blue curves); Figure 12b and 12e represent pairwise energies of valine-valine beads (black dashed curve) and valine-lipid alkyl tails (magenta dashed curve); and Figure 12c and 12f, energetic contributions between CNO/NC3 beads and the lysine side chain beads (SC_{C+}) (red curves), phosphate- SC_{C+} (green curves), GL1- SC_{C+} (brown), and GL2- SC_{C+} (cyan). Comparing Figure 12 with Figure 10, the trend of every curve in Figure 10 is reversed in Figure 12, except for the blue curves or BB-BB pair interaction. That is, every evaluated pairwise interaction between the peptide and the bilayer in Figure 12 favors the unfolded state ($L_c > 40 \text{ \AA}$), whereas the same interaction pairs in Figure 10, favor the folded state ($Fr_{sheet} > 0.6$). The decrease in BB-BB interaction energy (blue curves) with decrease in L_c is an obvious and expected trend; lower the end-to-end distance, more compact the peptide, higher the intra-peptide interaction and lower the energies.

On comparing Figures 12a and 12d with Figure 10a, we can see that PO4-BB (green curves) interaction energy is lowest in the POPSnd system. This is due to a lack of serine dipoles in the head group region, as dipoles might electrostatically compete with PO4. We can also see that NC3 interacts more strongly with BB beads (red curves in Figure 12d), in comparison to CNO in pCG POPS and POPSnd (red curves in Figure 10a and Figure 12a, respectively), due to its point charge of +1. Therefore, backbone beads interact more strongly with (a) POPSnd, due to the lack of an electrostatic gradient in the head group region, and hence increased PO4-BB interaction, and (b) pCG POPC, due to higher NC3-BB interaction, along with PO4-BB interaction. Both PO4-BB and NC3/CNO-BB

energies in Figure 12a and 12d (red and green curves), are the lowest for extended peptide conformations on the bilayer surface ($L_c > 40 \text{ \AA}$). This could be because, in both these systems, the dipole or electrostatic interactions within POPSnd bilayer and within pCG POPC bilayer are lower than within pCG POPS. In the case of pCG POPS, the added dipoles facilitate stronger lipid-lipid interactions, which leads to cluster formation (see Figure 6). Therefore, in pCG POPS systems, a balance between intra-peptide backbone interaction and peptide backbone-bilayer interaction is achieved. On the other hand, in both pCG POPS and POPSnd systems, the peptide backbone-bilayer interaction is higher, leading to decreased intra-peptide interactions. This suggests that there is a subtle balance between these two competing interactions (intra-peptide and peptide-lipid), which a model must be able to capture, in order to be used to study membrane-induced peptide folding.

From Figure 12b, 12e and 10b, we see that the valine-valine pairwise energies (black dashed curve) are lowest for folded conformations in the pCG POPS system (by -15 kJ/mol in Figure 10b). However, the valine-alkyl energies (magenta dashed lines) are lower in the case of pCG-POPC (Figure 12b) and POPSnd (Figure 12b) by about the same amount of -15 kJ/mol . Therefore, the net hydrophobic interaction of SVS-1 (intra-peptide and peptide-alkyl tail) does not bias the folded sheet-like state or the unfolded-extended state.

There are two main distinctions between Figures 12c, 12f and 10c. First, the interaction energy between lysine side chains and phosphate beads (green curves) is lowest (around -410 kJ/mol) in the POPSnd system (Figures 12c), which could be attributed to an absence of electrostatic gradient in the head group region. It is also worthwhile to note that the lowest energy is when the peptide is extended ($L_c > 40 \text{ \AA}$). Second, the electrostatic repulsive energy between lysine side chains and choline (NC3) beads of pCG POPC (red curve in Figure 12f) destabilizes the membrane-bound state ($+80 \text{ kJ/mol}$). This repulsion between the head groups of pCG POPC and lysine residues could explain the time-lag in peptide-bilayer interactions seen in Figure S11b. However, the longer side chains of lysine residues and its charge distribution on the peptide, facilitates binding to even pCG POPC membranes. In our study, only one peptide is present in the system (Lipid:Peptide is 240:1). With higher concentration of the peptide, repulsive interaction between the peptide side chains (lysines) and pCG POPC is likely to be more pronounced. Binding of cationic β -hairpin AMPs to zwitterionic lipid membranes have been previously observed in protegrin-1 (PG-1) known to interact with both zwitterionic and anionic lipids^{73,74}. CMP, the cysteine deleted analog of tachyplesin, is known to bind weakly to zwitterionic POPC vesicles, but remain unfolded⁷⁵. CMP, like SVS-1, folds in the presence of anionic lipids, and is disordered in water. Cationic peptides like TAT⁷⁶⁻⁷⁹, poly-

arginine sequences^{80,81}, and penetratin^{77,82} are also known to bind to DOPC and DPPC lipid membranes. Atomistic free energy studies with OPLS forcefield predicts lysine and arginine residues to have favorable interfacial free energies of partition with DOPC bilayers⁸³. It is also important to remember that the SVS-1 peptide used in this study is mapped to our minimalistic CG model, where we have only one type of hydrophobic and charged residue. Therefore, valine and lysine residues in our simulation study essentially represent a hydrophobic and charged residue prototype and not the properties of the residue themselves.

Finally, the trend in Coulombic interaction of GL1 and GL2, both with lysines and phosphates in (a) pCG POPC is minimal and almost non-existent (brown and cyan solid curves in Figure 12d and 12f), and (b) absent in POPSnd. Although the LJ interactions of GL1 and GL2 show a decrease in energy values with increase in L_c , similar to most other peptide-lipid interactions (brown and cyan dashed curves in Figure 12d and 12f), this is largely because of the location of the peptide within the bilayer.

4 Conclusion

We have explored the role of lipid head group dipoles in structural and dynamical properties of an anionic (POPS) and zwitterionic (POPC) bilayer. We have done this by introducing polarization into polar coarse-grained lipid head group. The model has roots in the MARTINI force field and has been built to be compatible with our recently developed protein model that captures *de novo* folding of secondary and supersecondary protein structures³⁶. Our model is slightly more expensive in computational cost. In simulations of the benchmark system with 240 POPC lipids and 7757 CG water molecules, our model is slowed down approximately by a factor of two in comparison with the MARTINI system, which mostly arises from the shorter time step in our model. Several interactions involving polarizable CG beads have been re-parametrized. It should also be noted that, we have not tested all the bead types of the MARTINI force field, and our lipid model is not transferable to the other lipid types, because it is intended to be used specifically with our peptide model to study membrane-induced peptide folding.

The physical properties of the POPS and POPC bilayers which formed spontaneously from a random configuration, exhibit reasonable descriptions of lipid behavior. To examine the performance of our model, we explored structural, dynamic and electrostatic properties, such as the cross-bilayer density profile, area per lipid, bilayer thickness, mean squared displacements, line tension, dipole potential, dielectric profile, head group orientation and formation of lipid clusters. Comparison of these properties with experiments and/or all-atom simulations shows good agreement. Our model also cap-

tures the right trend in membrane interface electrical potential, which the MARTINI model fails to capture.

The model predicts formation of lipid clusters in PS bilayers in agreement to all-atom simulations, but in contrast to the the MARTINI model. In particular, we have shown that dipole interactions are crucial in stabilizing lipid cluster formation in PS bilayers by mimicking the hydrogen bonding network present in the head group region of atomistic PS bilayers. The presence of PS lipid cluster formation causes a distinction in area per lipid between POPC and POPS bilayer in our model. That is, the presence of head group dipoles in POPS results in a condensation effect by the alignment of headgroup dipoles, which manifests as a decrease in area per lipid. In addition, the model indicates, in agreement with all-atom data, that the serine group lies at the same vertical position of the phosphate group. This is in contrast to the MARTINI model where the serine is found above the phosphate position. Also, more subtle changes to head groups, on interaction with monovalent ions are observed. With the addition of 1M NaCl, area per lipid of both POPS and POPC bilayers decreased due to an electrostatic condensation effect, and the average number of ion bridges formed between lipids increased. We are currently working on parameterizing ions and charged interactions based on size to charge ratio. In this model, all ions are considered as hydrated ions, with decrease in ion radius, there is also a change in the size of its hydration shell, thus by making this distinction we will be able to distinguish different types of monovalent ions.

We studied POPS mediated folding of anticancer peptide SVS-1 to explore the effects of lipid head group interactions in membrane-induced peptide folding. With pCG, we were able to observe membrane mediated folding of SVS-1 into β -hairpin with anionic bilayers, in agreement with experimental observations. The driving forces involved in folding include PO4-lysine interaction, valine-alkyl interaction, intra-peptide interaction and CNO-peptide interaction. PO4-lysine interaction contributes in attracting the peptide to the anionic bilayer, while valine-alkyl interaction and intra-peptide interaction play a role in stabilizing the β -turn conformation. We do not observe SVS-1 folding with pCG POPC, POPSnd, or in water, where it is intrinsically disordered. This is in agreement with experimental studies⁸.

One of the reasons we observe SVS-1 folding in pCG POPS bilayers, and not pCG POPC or POPSnd is because, a subtle balance between intra-peptide interaction (BB-BB) and peptide-lipid bilayer (BB-PO4 and BB-CNO) interaction is achieved only with pCG POPS. In the case of pCG POPC and POPSnd, the peptide-lipid interactions are more stronger (BB-PO4 in POPSnd and, BB-PO4 along with BB-NC3 in pCG POPC), thus decreasing intra-peptide interactions (BB-BB). The presence of added dipole particles in the CNO or serine head group region in pCG POPS, leads to higher

lipid-lipid interaction, which is also the primary reason for head-group mediated lipid clusters observed in these bilayers. This causes lower lipid-peptide interactions and subsequently, higher intra-peptide interactions. Whereas, both in the case of POPSnd and pCG POPC, there is less (if any) dipole-dipole interaction between lipids in a bilayer, which leads to increased peptide-lipid interaction and hence decreased intra-peptide interaction. This is also the reason clusters are not formed with MARTINI force field or in pCG POPC bilayers. The role played by the ester groups (GL1 and GL2) in all three systems (pCG POPS, pCG POPC, POPSnd) is minimal for SVS-1 peptide. There is also a lag in peptide-bilayer interaction for pCG POPC system, due to electrostatic repulsion between lysine residues and positively charged choline beads.

In conclusion, our results also suggest that there is an intricate balance between intra-peptide, peptide-lipid and lipid-lipid dipole interactions, which our CG model captures. We are currently investigating the effect of mixed POPC-POPS bilayers in SVS-1 folding. We are also planning in the near future to adapt our model to the polarizable water model developed by Wu et al. which better captures the experimental observables in water⁸⁰.

5 Acknowledgements

This research was supported in part by the UMD-NCI Cancer Partnership for Cancer Technology and by the National Science Foundation under the Grant CHE-1454948 and through XSEDE resources provided by the Texas Advanced Computing Center (TACC) under the grant number TG-MCB120045. We also thank Joel P. Schneider, Scott Medina, James T. Kindt and Keon Reid for helpful discussions.

References

- P. A. Leventis and S. Grinstein, *Annu. Rev. Biophys.*, 2010, **39**, 407–27.
- J. Schamberger and R. J. Clarke, *Biophys. J.*, 2002, **82**, 3081–3088.
- V. M. Aguilera and S. M. Bezrukov, *Eur. Biophys. J.*, 2001, **30**, 233–241.
- S. H. White, A. S. Ladokhin, S. Jayasinghe and K. Hristova, *J. Biol. Chem.*, 2001, **276**, 32395–32398.
- W. C. Wimley and S. H. White, *Nat. Struct. Mol. Biol.*, 1996, **3**, 842–848.
- A. S. Ladokhin and S. H. White, *J. Mol. Biol.*, 1999, **285**, 1363–1369.
- W. C. Wimley, K. Hristova, A. S. Ladokhin, L. Silvestro, P. H. Axelsen and S. H. White, *J. Mol. Biol.*, 1998, **277**, 1091–1110.
- C. Sinthuvanich, A. S. Veiga, K. Gupta, D. Gaspar, R. Blumenthal and J. P. Schneider, *J. Am. Chem. Soc.*, 2012, **134**, 6210–6217.
- E. Matyus, C. Kandt and D. P. Tieleman, *Curr. Med. Chem.*, 2007, **14**, 2789–2798.
- D. Lin and A. Grossfield, *Biophys. J.*, 2014, **107**, 1862–1872.
- D. Avrahami and Y. Shai, *Biochemistry*, 2002, **41**, 2254–2263.
- E. Gazit, I. R. Miller, P. C. Biggin, M. S. Sansom and Y. Shai, *J. Mol. Biol.*, 1996, **258**, 860–870.
- P. F. Almeida, A. S. Ladokhin and S. H. White, *Biochim. Biophys. Acta, Biomembr.*, 2012, **1818**, 178–182.
- E. M. Tytler, G. Anantharamaiah, D. E. Walker, V. K. Mishra, M. Palgunachari and J. P. Segrest, *Biochemistry*, 1995, **34**, 4393–4401.
- K. Matsuzaki, K. Sugishita, N. Fujii and K. Miyajima, *Biochemistry*, 1995, **34**, 3423–3429.
- P. J. Hoogerbrugge and J. M. V. A. Koelman, *Europhys. Lett.*, 2007, **19**, 155–160.
- R. Z. Khaliullin and T. D. Kühne, *Phys. Chem. Chem. Phys.*, 2013, **15**, 15746–66.
- W. Zhao, T. Róg, A. A. Gurtovenko, I. Vattulainen and M. Karttunen, *Biophys. J.*, 2007, **92**, 1114–24.
- A. Martín-Molina, C. Rodríguez-Beas and J. Faraudo, *Biophys. J.*, 2012, **102**, 2095–103.
- J. Pan, X. Cheng, L. Monticelli, F. A. Heberle, N. Kučerka, D. P. Tieleman and J. Katsaras, *Soft Matter*, 2014, **10**, 3716–25.
- J. N. Sachs, H. Nanda, H. I. Petrache and T. B. Woolf, *Biophys. J.*, 2004, **86**, 3772–82.
- S. A. Pandit and M. L. Berkowitz, *Biophys. J.*, 2002, **82**, 1818–27.
- J. M. Boettcher, R. L. Davis-Harrison, M. C. Clay, A. J. Nieuwkoop, Y. Z. Ohkubo, E. Tajkhorshid, J. H. Morrissey and C. M. Rienstra, *Biochemistry*, 2011, **50**, 2264–2273.
- P. Mukhopadhyay, L. Monticelli and D. P. Tieleman, *Biophys. J.*, 2004, **86**, 1601–1609.
- S.-J. Lee, Y. Song and N. A. Baker, *Biophys. J.*, 2008, **94**, 3565–3576.
- M. Menke, V. Gerke and C. Steinem, *Biochemistry*, 2005, **44**, 15296–15303.
- M. Venturoli, M. M. Sperotto, M. Kranenburg and B. Smit, *Phys. Rep.*, 2006, **437**, 1–54.
- Q. Waheed, R. Tjörnhammar and O. Edholm, *Biophys. J.*, 2012, **103**, 2125–2133.
- H. J. Risselada and S. J. Marrink, *Proc. Natl. Acad. Sci. U. S. A.*, 2008, **105**, 17367–17372.
- M. J. Stevens, *J. Chem. Phys.*, 2004, **121**, 11942–11948.
- Z.-J. Wang and M. Deserno, *New journal of physics*, 2010, **12**, 095004.
- E. M. Curtis and C. K. Hall, *J. Phys. Chem. B*, 2013, **117**, 5019–5030.
- C. F. Lopez, S. O. Nielsen, G. Srinivas, W. F. DeGrado and M. L. Klein, *J. Chem. Theory Comput.*, 2006, **2**, 649–655.
- S. J. Marrink, H. J. Risselada, S. Yefimov, D. P. Tieleman and A. H. De Vries, *J. Phys. Chem. B*, 2007, **111**, 7812–7824.
- L. Monticelli, S. K. Kandasamy, X. Periole, R. G. Larson, D. P. Tieleman and S. J. Marrink, *J. Chem. Theory Comput.*, 2008, **4**, 819–834.
- S. J. Ganesan and S. Matysiak, *J. Chem. Theory Comput.*, 2014, **10**, 2569–2576.
- S. O. Yesylevskyy, L. V. Schäfer, D. Sengupta and S. J. Marrink, *PLoS Comput. Biol.*, 2010, **6**, e1000810.
- D. Gaspar, A. S. Veiga, C. Sinthuvanich, J. P. Schneider and M. A. R. B. Castanho, *Biochemistry*, 2012, **51**, 6263–6265.
- K. Gupta, H. Jang, K. Harlen, A. Puri, R. Nussinov, J. P. Schneider and R. Blumenthal, *Biophys. J.*, 2013, **105**, 2093–2103.
- B. R. Brooks, R. E. Bruccoleri, B. D. Olafson, D. J. States, S. Swaminathan and M. Karplus, *J. Comput. Chem.*, 1983, **4**, 187–217.
- G. Bellesia, A. I. Jewett and J. E. Shea, *Protein Sci.*, 2010, **19**, 141–154.
- B. Hess, C. Kutzner, D. Van Der Spoel and E. Lindahl, *J. Chem. Theory Comput.*, 2008, **4**, 435–447.
- W. Humphrey, A. Dalke and K. Schulten, *J. Mol. Graphics*, 1996, **14**, 33–38.
- S. Nosé, *J. Chem. Phys.*, 1984, **81**, 511–519.
- W. Hoover, *Phys. Rev. A*, 1985, **31**, 1695–1697.
- M. Parrinello and A. Rahman, *J. Appl. Phys.*, 1981, **52**, 7182–7190.
- T. Darden, D. York and L. Pedersen, *J. Chem. Phys.*, 1993, **98**, 10089–10092.
- B. Hess, H. Bekker, H. J. Berendsen and J. G. E. M. Fraaije, *J. Comput. Chem.*, 1997, **18**, 1463–1472.

- 49 C. Oostenbrink, A. Villa, L. Mark and W. Van Gunsteren, *J. Comput. Chem.*, 2004, **25**, 1656–1676.
- 50 R. Kubo, M. Yokota and S. Nakajima, *J. Phys. Soc. Jpn.*, 1957, **12**, 1203–1211.
- 51 F. Y. Jiang, Y. Bouret and J. T. Kindt, *Biophys. J.*, 2004, **87**, 182–192.
- 52 A. A. Hagberg, D. A. Schult and P. J. Swart, Proceedings of the 7th Python in Science Conference (SciPy2008), Pasadena, CA USA, 2008, pp. 11–15.
- 53 A. Luzar and D. Chandler, *Nature*, 1996, **379**, 55–57.
- 54 A. A. Gurtovenko and I. Vattulainen, *J. Phys. Chem. B*, 2008, **112**, 4629–4634.
- 55 G. Cevc, A. Watts and D. Marsh, *Biochemistry*, 1981, **20**, 4955–4965.
- 56 N. Kučerka, M. P. Nieh and J. Katsaras, *Biochim. Biophys. Acta, Biomembr.*, 2011, **1808**, 2761–2771.
- 57 N. Kučerka, Y. Liu, N. Chu, H. I. Petrache, S. Tristram-Nagle and J. F. Nagle, *Biophys. J.*, 2005, **88**, 2626–2637.
- 58 B. König, U. Dietrich and G. Klöse, *Langmuir*, 1997, **13**, 525–532.
- 59 J. M. Smaby, M. M. Momsen, H. L. Brockman and R. E. Brown, *Biophys. J.*, 1997, **73**, 1492–1505.
- 60 J. Aittoniemi, P. S. Niemelä, M. T. Hyvönen, M. Karttunen and I. Vattulainen, *Biophys. J.*, 2007, **92**, 1125–1137.
- 61 R. A. Böckmann, A. Hac, T. Heimburg and H. Grubmüller, *Biophys. J.*, 2003, **85**, 1647–1655.
- 62 P. Jurkiewicz, L. Cwiklik, A. Vojtíšková, P. Jungwirth and M. Hof, *Biochim. Biophys. Acta, Biomembr.*, 2012, **1818**, 609–616.
- 63 R. M. Venable, Y. Luo, K. Gawrisch, B. Roux and R. W. Pastor, *The Journal of Physical Chemistry B*, 2013, **117**, 10183–10192.
- 64 J.-X. Cheng, S. Pautot, D. A. Weitz and X. S. Xie, *Proc. Natl. Acad. Sci. U. S. A.*, 2003, **100**, 9826–9830.
- 65 M. Orsi, D. Y. Haubertin, W. E. Sanderson and J. W. Essex, *J. Phys. Chem. B*, 2008, **112**, 802–815.
- 66 S. J. Slater, C. Ho, F. J. Taddeo, M. B. Kelly and C. D. Stubbs, *Biochemistry*, 1993, **32**, 3714–3721.
- 67 D. V. Zhelev and D. Needham, *Biochim. Biophys. Acta, Biomembr.*, 1993, **1147**, 89–104.
- 68 E. Karatekin, O. Sandre, H. Guitouni, N. Borghi, P.-H. Puech and F. Brochard-Wyart, *Biophys. J.*, 2003, **84**, 1734–1749.
- 69 S. Kamtekar, J. M. Schiffer, H. Xiong, J. M. Babik and M. H. Hecht, *Science*, 1993, **262**, 1680–1685.
- 70 Y. Shai, *Biochim. Biophys. Acta, Biomembr.*, 1999, **1462**, 55–70.
- 71 S. H. White and W. C. Wimley, *Annu. Rev. Biophys. Biomol. Struct.*, 1999, **28**, 319–365.
- 72 H. Sato and J. B. Feix, *Biochim. Biophys. Acta, Biomembr.*, 2006, **1758**, 1245–1256.
- 73 Y. Ishitsuka, D. S. Pham, A. J. Waring, R. I. Lehrer and K. Y. C. Lee, *Biochim. Biophys. Acta, Biomembr.*, 2006, **1758**, 1450–1460.
- 74 T. Lazaridis, Y. He and L. Prieto, *Biophys. J.*, 2013, **104**, 633–642.
- 75 A. Ramamoorthy, S. Thennarasu, A. Tan, K. Gottipati, S. Sreekumar, D. L. Heyl, F. Y. An and C. E. Shelburne, *Biochemistry*, 2006, **45**, 6529–6540.
- 76 H. D. Herce and A. E. Garcia, *Proc. Natl. Acad. Sci. USA*, 2007, **104**, 20805–20810.
- 77 S. Yesylevskyy, S.-J. Marrink and A. E. Mark, *Biophys. J.*, 2009, **97**, 40–49.
- 78 S. Kawamoto, M. Takasu, T. Miyakawa, R. Morikawa, T. Oda, S. Futaki and H. Nagao, *Mol. Simul.*, 2012, **38**, 366–368.
- 79 K. Akabori, K. Huang, B. W. Treece, M. S. Jablin, B. Maranville, A. Woll, J. F. Nagle, A. E. Garcia and S. Tristram-Nagle, *Biochim. Biophys. Acta, Biomembr.*, 2014, **1838**, 3078–3087.
- 80 Z. Wu, Q. Cui and A. Yethiraj, *J. Phys. Chem. B*, 2010, **114**, 10524–10529.
- 81 H.-L. Lee, E. Dubikovskaya, H. Hwang, A. Semyonov, H. Wang, L. Jones, R. Twieg, W. Moerner and P. Wender, *J. Am. Chem. Soc.*, 2008, **130**, 9364–9370.
- 82 Z. Salamon, G. Lindblom and G. Tollin, *Biophys. J.*, 2003, **84**, 1796–1807.
- 83 J. L. MacCallum, W. D. Bennett and D. P. Tieleman, *Biophysical journal*, 2008, **94**, 3393–3404.